Research Square

Preprints are preliminary reports that have not undergone peer review.
They should not be considered conclusive, used to inform clinical practice,
or referenced by the media as validated information.

Laboratory and Field Performance Assessment of LPWA Tilt Sensors for Slope Monitoring and Disaster Early Warning

Ryosuke Miyake
Ehime University
Tomoki Nakazora
Kyoto University
Naoki Kinoshita
Ehime University
Hideaki Yasuhara
yasuhara.hideaki.7p@kyoto-u.ac.jp

Kyoto University

Research Article

Keywords: LPWA, Tilt sensor, Slope monitoring, Landslide prediction

Posted Date: March 6th, 2026

DOI: https://doi.org/10.21203/rs.3.rs-9001528/v1

License: This work is licensed under a Creative Commons Attribution 4.0 International License.
Read Full License

Additional Declarations: No competing interests reported.

Laboratory and Field Performance Assessment of LPWA Tilt Sensors for Slope Monitoring and Disaster Early Warning

Ryosuke Miyake[1], Tomoki Nakazora[2], Naoki Kinoshita[1], Hideaki Yasuhara[2*]

[1] Department of Civil and Environmental Engineering, Ehime University, Matsuyama, 790-8577, JAPAN.

[2] Department of Urban Management, Kyoto University, Kyoto, 615-8540, JAPAN.

*Corresponding Author: yasuhara.hideaki.7p@kyoto-u.ac.jp

Abstract

This study evaluated the performance of tilt sensors equipped with Low-Power Wide-Area (LPWA) communication through controlled laboratory experiments and extensive field observations on natural slopes. Eight tilt sensors (A–H), varying in resolution, accuracy, installation type, and communication protocol, were examined. In the laboratory, a high-precision testing machine was used to apply precise tilt angles (0.0001º resolution, 0.0002º accuracy), enabling the quantitative assessment of each axis. Sensor accuracy was specifically evaluated using the 3σ (three-sigma) criterion as an index of noise, and Tilt Sensor A was found to exhibit the highest precision. Field observations at

three sites in Japan assessed the influence of environmental factors, such as rainfall and temperature, on the tilt sensors' long-term stability. Composite tilt angles and inclination rates were derived from the data to quantify slope deformation. Buried Tilt sensors demonstrated high stability with minimal susceptibility to temperature effects, while above-ground tilt sensors with coarser resolution were more significantly affected by external conditions. At Site A, the tilt sensors successfully captured slope failure—from initial creep to accelerated deformation—demonstrating their effectiveness as early warning indicators. The observed relationship between the inclination rate and the remaining time to failure was consistent with previous findings. Crucially, a strong correlation was found between the catalog-specified accuracy and the field-observed noise level, indicating that tilt sensor accuracy reliably predicts field stability. These results provide essential, practical insights for the selection and operation of tilt sensors in slope monitoring and early warning systems.

Keywords: LPWA, Tilt sensor, Slope monitoring, Landslide prediction.

1. Introduction

Japan’s geophysical setting—characterized by steep terrain, fragile geology, and heavy rainfall—renders it highly vulnerable to sediment-related disasters such as

landslides and debris flows. Approximately 70% of the country consists of mountainous or hilly areas, and its rivers are notably shorter and steeper in comparison to global standards. These conditions, compounded by seasonal heavy rain during the rainy season and typhoon events, have historically led to frequent flooding and slope failures (Yoshimura et al. 2005).

Climate change has further intensified the risk of such disasters. The Automated Meteorological Data Acquisition System (AMeDAS), operated by the Japan Meteorological Agency, comprises approximately 1,300 observation stations across Japan and has provided high-density precipitation data since the late 1970s. Analyses based on AMeDAS data indicate an increasing trend in the annual frequency of heavy rainfall events in Japan, highlighting recent changes in precipitation characteristics (Japan Meteorological Agency 2024). Consistent with this trend, the Annual Report on Sediment-related Disasters in Japan, together with related research by the National Institute for Land and Infrastructure Management (NILIM), reports that the annual average number of sediment disasters in Japan increased by approximately 1.5 times between 2010 and 2019, reflecting the influence of intensified heavy rainfall and extreme weather events (Takayuki 2021). The Sediment Disasters in Japan in 2024 report documents 1,433 sediment-related disasters across Japan in 2024, resulting in 56 fatalities

55 and extensive damage to residential areas, demonstrating the continuing severity and
56 nationwide impact of recent sediment hazards (Ministry of Land, Infrastructure, Transport
57 and Tourism 2025). These figures illustrate the urgency of developing technologies for
58 early detection and warning to minimize human and economic losses. Landslides
59 typically occur when rainfall increases pore water pressure within the slope, thereby
60 reducing soil strength (Turner and Schuster 1996). While rainfall-based empirical models
61 have been used to predict such events, they often fall short due to the complex interplay
62 of rainfall, soil characteristics, topography, and antecedent moisture. Thus, systems
63 capable of directly monitoring slope deformations are considered more effective for
64 hazard assessment.

65 Conventional systems for slope monitoring generally utilize wired sensors such as
66 tilt sensors or real-time kinematic GNSS(Global Navigation Satellite System). However,
67 such systems are expensive to install and maintain and require on-site data retrieval,
68 which limits their applicability in remote and wide-area monitoring. Although recent
69 advances in GNSS and satellite-based monitoring have enabled some progress toward
70 real-time observation (Ito et al. 2005), achieving comprehensive coverage remains
71 economically and logistically challenging. Hence, cost-effective, autonomous, and
72 scalable monitoring systems are essential.

Low-Power Wide-Area (LPWA) communication has emerged as a promising solution for such applications. LPWA networks are designed to support long-range communication with low power consumption and low data rates, making them well suited for large-scale IoT deployments compared with conventional short-range or cellular technologies (Mekki et al. 2019). These features make LPWA particularly compatible with slope monitoring systems, especially in mountainous regions where regular maintenance and stable power supply are difficult. Because slope monitoring typically requires the transmission of only small data packets at infrequent intervals, the lower data rate of LPWA is not a critical limitation.

Since 2022, the Shikoku CX initiative has deployed LPWA-enabled tilt sensors on natural slopes in and around Ehime Prefecture to conduct long-term geotechnical monitoring (Ehime University 2023; TryAngle Ehime 2023). In parallel, previous studies have employed tilt rate (angular velocity) as a threshold parameter in early warning systems for slope instability based on tilt sensor monitoring (Uchimura et al. 2015; Sheikh et al. 2021; Wang et al. 2022). Such systems define multiple alert levels based on tilt-rate thresholds, typically ranging from 0.02°/h to 1.0°/h, to support phased evacuation decisions. Although recent large-scale analyses of IoT tilt-sensor data have proposed provisional management thresholds (Tanigawa and Slope Monitoring Market

Development Consortium 2024), there remains a lack of systematic evaluation of whether commercially available sensor technologies can reliably detect these thresholds under real-world field conditions. In particular, uncertainties remain regarding the required resolution, long-term stability under environmental variability, and optimal installation strategies.

To address these gaps, this study evaluates the practical performance of several LPWA-compatible commercial tilt sensors through laboratory and field experiments. The laboratory tests assess each sensor's resolution, accuracy, and temperature sensitivity. The field monitoring, conducted across three landslide-prone areas (Site W, Site M, and Site A), provides year-long observational data to examine sensor responsiveness, correlation with rainfall, and the validity of the proposed warning thresholds. This study aims to provide practical insight into the design and deployment of LPWA-based slope monitoring systems, contributing to the advancement of robust, cost-effective early warning networks for sediment-related hazards.

2. Monitoring System and Methods

2.1. Sensor Installation Locations

Tilt sensors were strategically installed at geologically critical locations to capture early signs of slope instability. Two primary installation targets were identified: compressive zones within known landslides and zero-order basins.

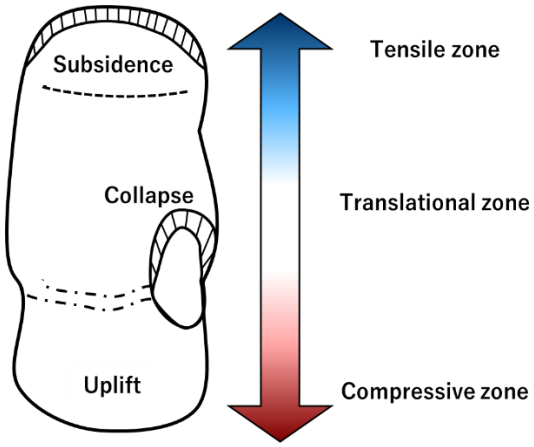


Figure 1. Landslide zone schematic diagram

Compressive zones, illustrated in Figure 1, are areas where the landslide mass accumulates and is pushed forward. These zones are prone to surface cracking due to internal compression and represent locations of elevated failure potential. Accordingly, tilt sensors were placed in these regions to enable early detection of accelerating movement.

117 Zero-order basins (ZOBs) were also prioritized as installation sites. ZOBs are
118 defined as unchanneled headwater hollows located upstream of first-order streams in the
119 Horton stream classification system and represent geomorphic units corresponding to the
120 earliest stage of valley development controlled by erosional processes (Horton 1945;
121 Tsukamoto et al. 1973). ZOBs can be identified on topographic maps where the concavity
122 between contour lines has a length-to-width ratio less than one (Figure 2) (National
123 Institute for Land and Infrastructure Management 2016). These basins act as nascent
124 water catchments and are often implicated in slope failure due to their tendency to
125 promote infiltration and subsurface saturation.
126

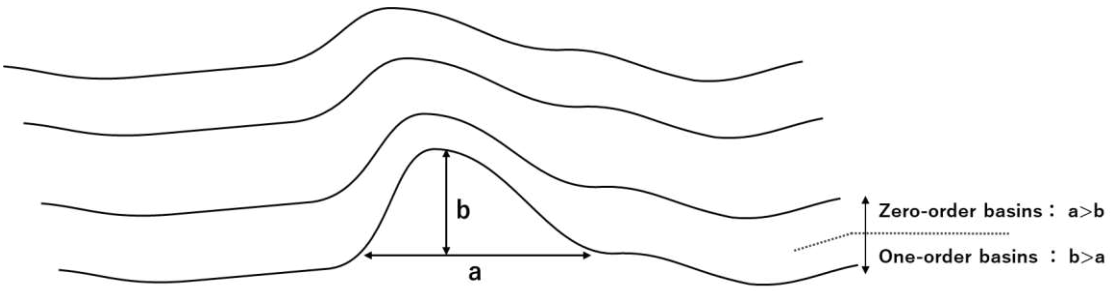


Figure 2. Zero-order basins diagram modified from (National Institute for Land and Infrastructure Management 2016)

127
128 The rationale for monitoring ZOBs stems from the concept that headwater hollows
129 evolve over time, and collapse events occurring in ZOBs represent the earliest signs of

130 watershed development (Tsukamoto 1973). Thus, ZOBs are highly predictive
131 topographies for early-stage deformation, and sensors installed in these areas can provide
132 vital early-warning data.
133 In summary, sensors were installed in:
134 • Compressive zones within landslide masses where cracks are likely to form;
135 • Zero-order basins are identifiable by geomorphic indicators on topographic maps.
136 These criteria ensured that the monitoring system was deployed in areas with the greatest
137 potential for detecting precursory deformation, thereby improving the overall efficacy of
138 early-warning system.
139

140 **2.2. Monitoring Workflow and Current Challenges**

141 Figure 3 illustrates the workflow of the LPWA-based slope monitoring system. Once
142 installed, each tilt sensor records two- or three-axis inclination angles (X, Y, and
143 optionally Z), along with temperature and humidity, at fixed intervals. These data are
144 transmitted wirelessly via LPWA base stations or directly to the cloud. Real-time
145 monitoring is enabled via PCs or mobile devices. However, a key challenge remains: the
146 lack of consensus on resolution and accuracy requirements for early-warning alerts.
147 Various tilt-rate thresholds have been proposed, such as 0.02 °/h for caution, and 1.0 °/h

for immediate evacuation (Tanigawa and Slope Monitoring Market Development Consortium 2024). Other thresholds include 0.01°/h for alerting, 0.1 °/h for evacuation preparation, and 1.0°/h for immediate evacuation (Wang et al. 2022). Other studies have proposed thresholds such as 0.11°/h (Uchimura et al. 2015) and 0.4°/h (Sheikh et al. 2021) for immediate evacuation. Sensors with insufficient resolution could trigger false alarms, thereby undermining system reliability. Thus, establishing minimum sensor performance standards is crucial.

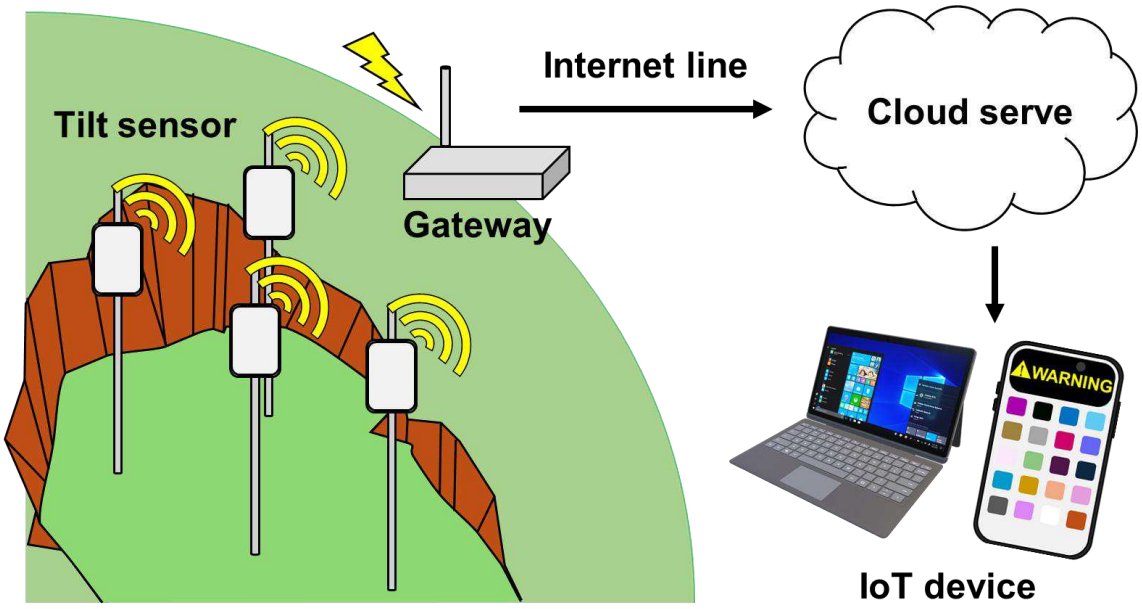


Figure 3. Process of slope monitoring utilizing LPWA-enabled tilt sensor

2.3. Overview of Tilt Sensors Evaluated

Seven LPWA-enabled tilt sensors (A through G) were evaluated through laboratory and field testing (Figures 4a to 4h). Each sensor varied in communication protocol, resolution, power source, and installation method. Key features include:

- **Tilt Sensor A** (Figure 4a)**:**

  LTE-M communication; 0.001° resolution; lithium battery lasting up to 5 years; buried installation; dynamic alert frequency (hourly or every 10 minutes) based on tilt-rate thresholds.

- **Tilt Sensor B** (Figure 4b)**:**

  LoRa communication; 0.02° resolution; D-cell battery; buried installation; alert levels defined by 0.05°/5h, 0.1°/h, and 1.0°/h.

- **Tilt Sensor C** (Figure 4c)**:**

  Sigfox communication; 0.06° resolution; surface-mounted; tilt alerts based on angle thresholds (±1°, ±5°); shock detection function included.

- **Tilt Sensor D** (Figure 4d)**:**

  Sigfox communication; 0.001° but reported in 0.005° increments; buried cylindrical installation; configurable alert transmission up to 140 times/day.

- **Tilt Sensor E** (Figure 4e)**:**

LoRa communication; 0.001° resolution; solar powered; surface-mounted; customizable transmission intervals.

- **Tilt Sensor F** (Figure 4f)**:**

  ZETA communication; 0.0002° resolution; AA batteries; surface-mounted; 3-axis capability; configurable threshold alerts.

- **Tilt Sensor G** (Figure 4g)**:**

  Sigfox communication; 0.1° resolution; manganese-lithium battery for >10 years; surface-mounted; alert triggered at 20° and 30° angles.

- **Tilt Sensor H** (Figure 4h)**:**

  NB-IoT communication; 0.01° resolution.

These basic specifications are summarized in Table 1.



Figure 4a. Tilt Sensor A



Figure 4b. Tilt Sensor B



Figure 4c. Tilt Sensor C



Figure 4d. Tilt Sensor D



Figure 4e. Tilt Sensor E



Figure 4f. Tilt Sensor F



Figure 4g. Tilt Sensor G



Figure 4h. Tilt Sensor H

Table 1. Basic information on Tilt sensors

Tilt sensor	Resolution	Transmission Frequency	Installation Type	Communication Protocol
A	0.001º	1 minute	Buried	LTE-M
B	0.003º	1 minute	Buried	LoRa
C	0.06º	15 minutes	Above Ground	Sigfox
D	0.005º	15 minutes	Buried	Sigfox
E	0.001º	2 minutes	Above Ground	LoRa
F	0.0002º	1 minute	Above Ground	ZETA
G	0.1º	30 minutes	Above Ground	Sigfox
H	0.01º	5 minutes	Buried	NB-IoT

185 These sensors were deployed in various topographic and hydrologic contexts to
186 assess their real-world performance. Differences in resolution, battery life, and alert
187 functionality provided critical insights into the suitability of each model for monitoring
188 long-term slope disaster risk.
189

3. Laboratory Evaluation of LPWA Tilt Sensors

3.1. Basic Characteristics Test

This section presents the evaluation of the fundamental characteristics of tilt sensors through laboratory experiments. The tilt sensors examined in this study vary in terms of resolution, accuracy, external housing design, and installation methods. In field monitoring, multiple tilt sensors are often installed in proximity. However, because their observation points differ, conducting a fully quantitative evaluation is challenging. Therefore, this laboratory experiment was conducted to quantitatively assess the performance of multiple tilt sensors by applying controlled inclination angles using a dedicated apparatus.

3.2. Apparatus

This section describes the apparatus used in the experiments. Figure 5 presents an external view of the apparatus. The apparatus is capable of applying arbitrary inclination angles to the tilt sensors. Specifically, the base features a seesaw-like mechanism, with a spring exerting upward force from below and a micrometer applying downward force from above. By finely adjusting the micrometer to balance these opposing forces, the base can be inclined to a precise angle.

208

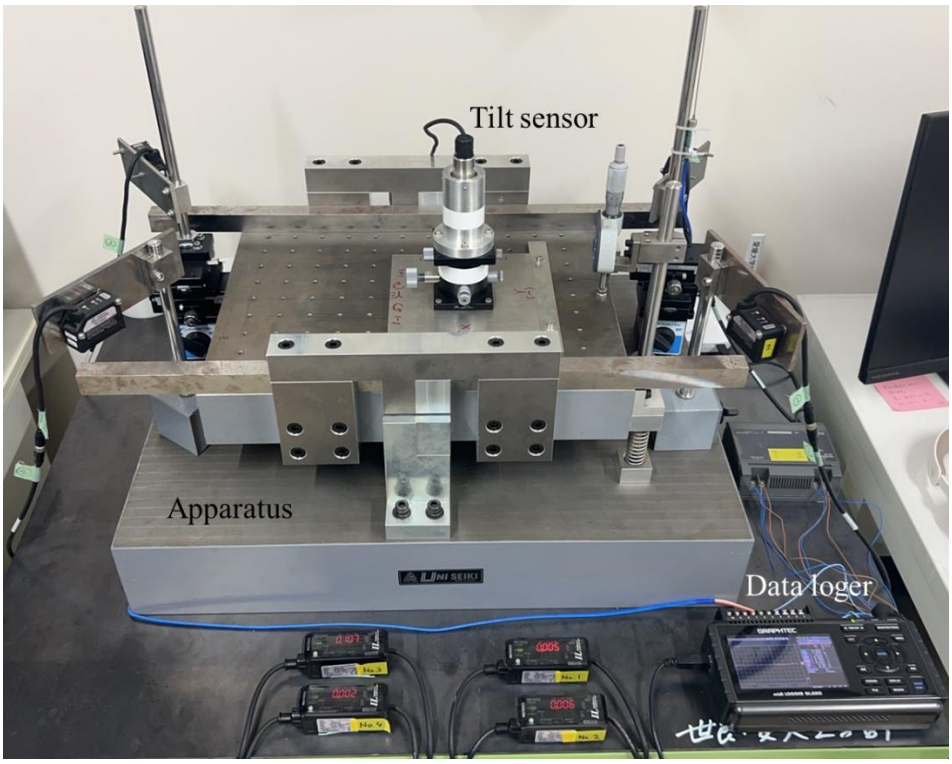


Figure 5. Appearance of the apparatus

209

210 The displacement measured by laser displacement sensors is converted into
211 inclination angles as follows. Four laser displacement sensors (KEYENCE: IL-030,
212 resolution 0.001 mm, repeatability 0.001 mm) were installed at the four corners of the
213 apparatus. As shown in Figure 6, the pair of sensors on the near side measured
214 displacement relative to the initial horizontal position, while the pair on the far side
215 measured displacement in the same manner. The average inclination calculated from these
216 two sensor pairs was defined as the inclination angle applied by the apparatus. Figures 7

217 and 9 illustrate the procedure for converting the measured displacement into inclination

218 using Eq. (1).

$$\theta = \tan^{-1}\left(\frac{l_2 - l_1}{L}\right) \quad (1)$$

219 where θ [º] is the inclination of the base, l_1 and l_2 [mm] are measured distances of the

220 two sensors shown in Figure 6, L [mm] is the horizontal distance between a pair of

221 sensors.

222

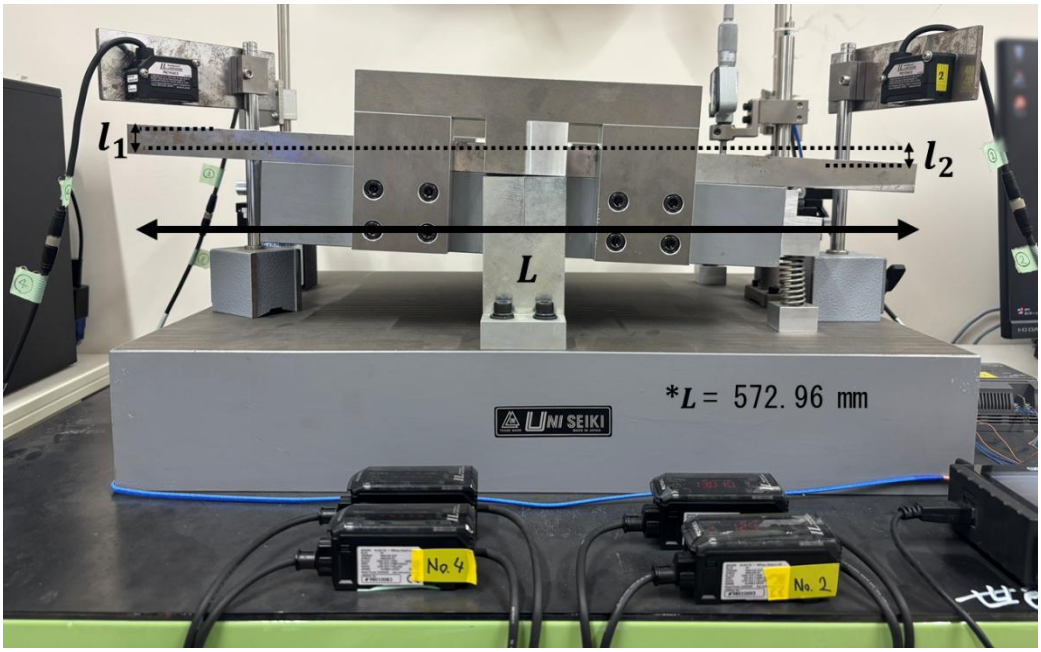


Figure 6. Diagram of tilt angle conversion

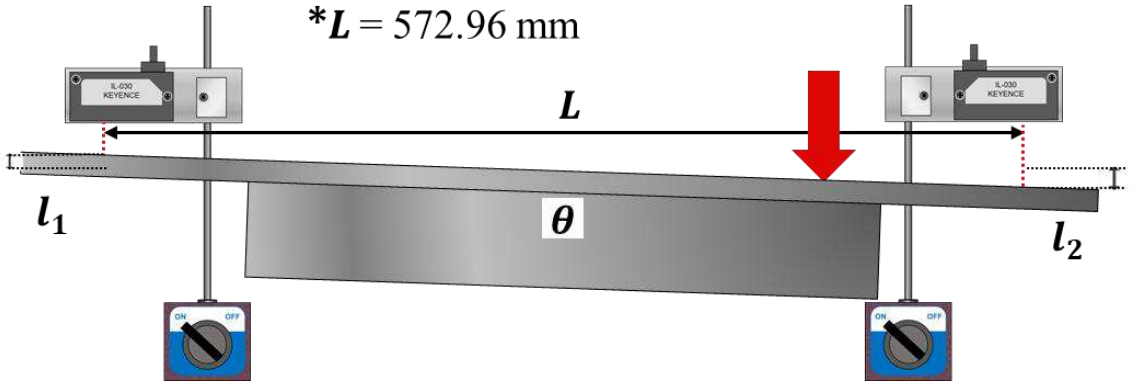


Figure 7. Illustration of the apparatus

223

224 Regarding the resolution and accuracy of the apparatus: Applying Eq. (1), a
225 displacement of 0.001 mm corresponds to an inclination of 0.0001º. Hence, the resolution
226 of the apparatus is 0.0001º. The accuracy was verified by setting the apparatus to a
227 horizontal position using a precision level (Obishi Keiki Seisakusho Co., Ltd., AC101,
228 accuracy: 0.020 mm/m) and leaving it undisturbed for approximately 14 hours at a
229 controlled temperature of 22°C. The standard deviation (3σ) of the measured inclination
230 was ±0.0002º (Figure 8). Therefore, for this study, the resolution of the apparatus is
231 considered to be 0.0001º, and the accuracy is ±0.0002º.

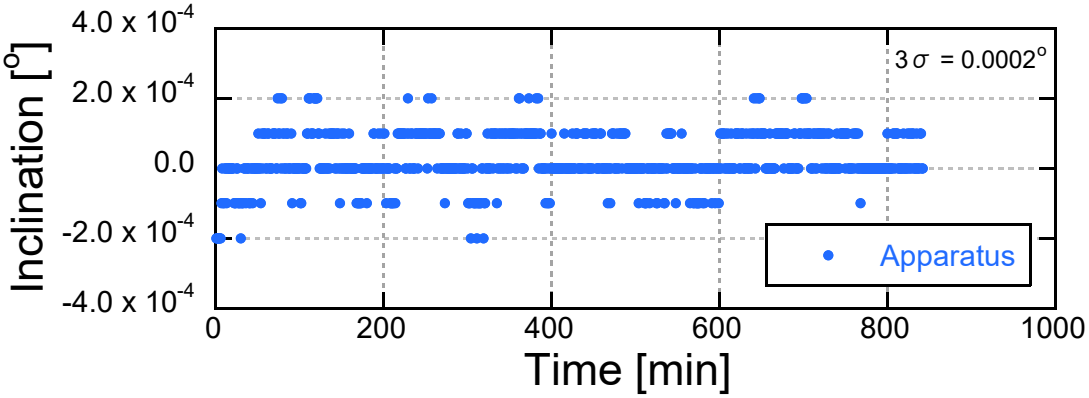


Figure 8. Accuracy of the laboratory apparatus

232

233 **3.3. Experimental Method**

234 This section describes the method used to evaluate the performance of the tilt sensors
235 using the apparatus. A constant inclination angle is applied to the tilt sensors via the
236 apparatus, while inclination measurements are simultaneously recorded from the tilt
237 sensors. A conceptual diagram of the experiment is shown in Figure 9. By comparing the
238 prescribed inclination angle with the inclination angle observed by the tilt sensor, the
239 performance of each tilt sensor can be quantitatively assessed. The procedure is as
240 follows:

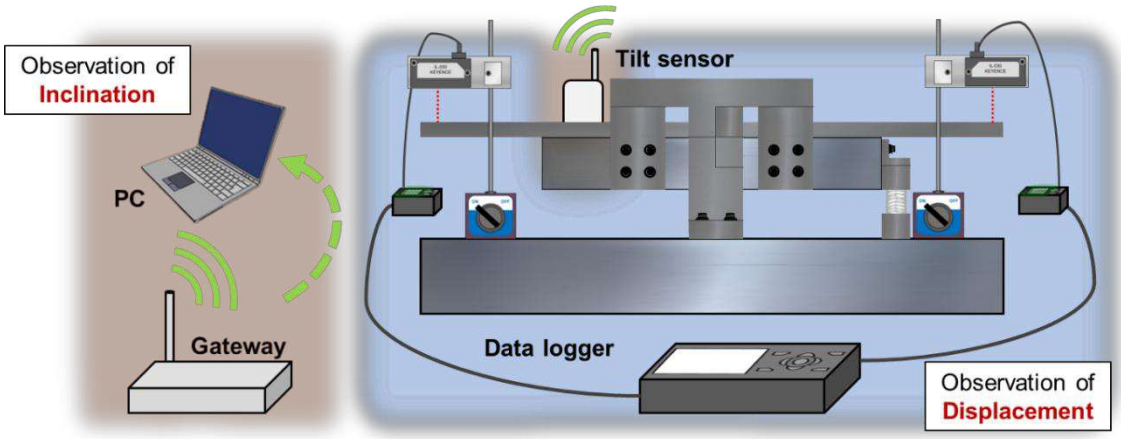


Figure 9. Schematic diagram of the entire experimental setup

241

242 **3.3.1. Installation of Tilt Sensor**

243 To prevent observation errors caused by temperature fluctuations, the room temperature
244 was maintained at 23 ± 1.0 °C using air conditioning, and the system was stabilized for
245 more than 12 hours before starting the test. The laser displacement sensors were cleaned
246 with compressed air to remove any dust. Two positioning brackets were mounted on the
247 base using a precision square (Ohishi Keiki Seisakusho Co., Ltd., FB102) to ensure
248 orthogonal alignment (Figure 10). The test tilt sensor was mounted on a steel plate,
249 powered on, and aligned along the brackets such that the X-axis of the tilt sensor was
250 parallel to the long side of the base and oriented toward the micrometer (Figure 11).

251

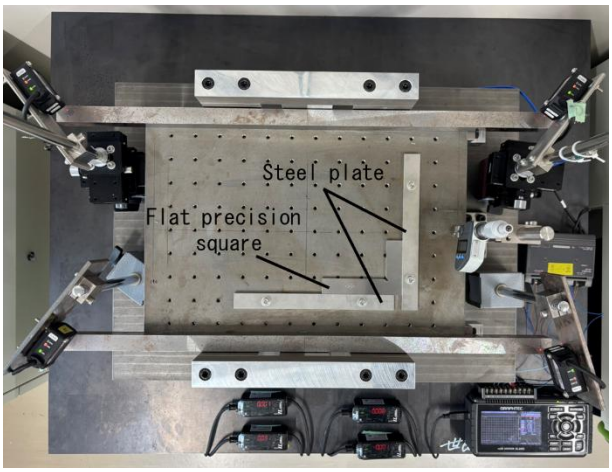


Figure 10. Preparation for Tilt sensor installation

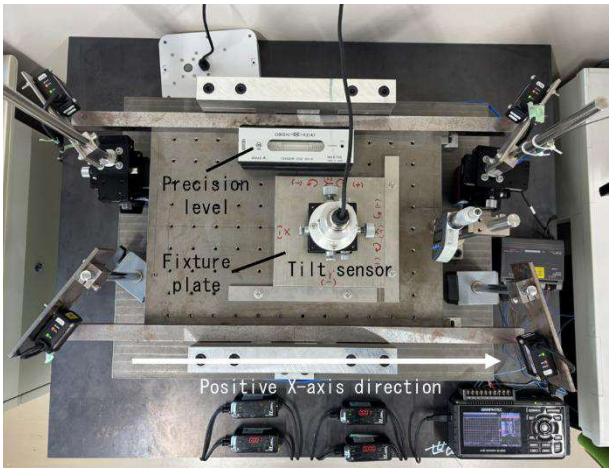


Figure 11. Initial condition of the experiment

252

253 **3.3.2. Initial Setup**

254 A precision level (accuracy: 0.020 mm/m) was placed at the center of the base, and the

255 micrometer was adjusted to achieve a horizontal position (Figure 11). The level was then

removed, and the four laser displacement sensors were set to zero.

3.3.3. Data Acquisition Setup

A PC was connected to a data logger (Graphtec Co., midi LOGGER GL220), and the application software (GL100_240_840_APS) was used to initiate the recording of laser sensor data. Real-time conversion and plotting of inclination were performed in Excel using Eq. (1) (Figure 12).



Figure 12. Real-time inclination from the apparatus

3.3.4. Experiment Execution

The tilt sensors were kept in a horizontal position for several hours to ensure stable data

transmission and sensor voltage. The inclination was then increased stepwise using the micrometer first in increments of 0.001º up to 0.020º, and then in increments of 0.010º up to 0.050º (Figure 13). The final inclination was maintained for several hours before ending the test. For tilt sensors with short data transmission intervals, micrometer adjustments were made every three transmissions, excluding the first reading and averaging the next two. For tilt sensors with longer intervals, the average of two consecutive readings was used (Figure 14).

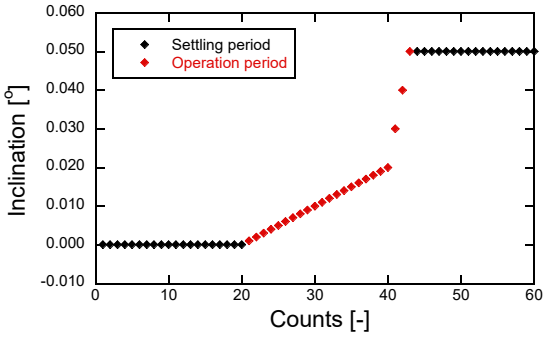


Figure 13. Method of applying inclination

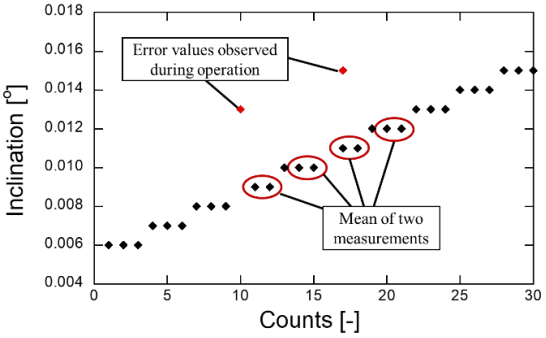


Figure 14. Removal of error data

3.3.5. **Evaluation Method**

The converted inclination obtained from Eq. (1) was used to evaluate the accuracy of the tilt sensors. First, a scatter plot was generated to compare the inclination angles measured

simultaneously by the tilt sensor and the laser displacement sensors, allowing for an assessment of linearity between the two datasets. Next, Eqs. (2) and (3) were applied to quantify the variation between the inclination angles measured by the tilt sensor and the actual inclination angles imposed by the laboratory test apparatus. This variation was evaluated using the standard deviation (3σ) to quantitatively assess the dispersion of the measurements.

$$\boldsymbol{e_i} = |\boldsymbol{\theta_i} - \boldsymbol{\theta_i'}| \tag{2}$$

$$\boldsymbol{\sigma} = \sqrt{\frac{\sum_{i=1}^{n}(\boldsymbol{e_i} - \mu)^2}{\boldsymbol{n}}} \tag{3}$$

Where e_i [º] is the absolute difference between observed and applied inclination, θ_i [º] is observed inclination, θ_i' [º] is applied inclination, σ [º] is standard deviation, μ [º] is the mean of e_i.

Based on the evaluation method described above, the results were categorized into two types of analysis: Type A and Type B, as described below. In the Type A results, the inclination angles set by the laboratory test apparatus (Inclination) were plotted as square markers, while the inclination angles measured by the tilt sensors (X-axis) were plotted as red circles. When the tilt sensor accurately measured the applied inclination, the red circles overlapped with the square markers, indicating high accuracy (see Figure 15). In

294 the Type B results, the variation between the tilt sensor measurements and the applied
295 inclination angles was analyzed. The horizontal axis represented the applied inclination
296 angles, while the vertical axis represented the inclination angles measured by the tilt
297 sensor. Ideally, the data points aligned along the 45° reference line, indicating a perfect
298 agreement. The 45° line was included in the figures, and the standard deviation (σ)
299 calculated using Eq. (3) was displayed on the graph to quantitatively represent the
300 measurement dispersion.
301
302 **3.4. Experimental Results**
303 Table 2 first summarizes the performance of all eight tilt sensors tested in the
304 laboratory. The table presents the standard deviations (3σ) for the inclination, strike, and
305 vertical components, and the sensors are ranked based on the standard deviation in the
306 inclination direction, from smallest to largest. Among these, tilt sensor A demonstrated
307 the smallest deviation and therefore the highest measurement accuracy.
308 Based on this ranking, tilt sensor A was selected as the representative example for
309 detailed analysis. The Type A results (Figure 15a), which compare the applied and
310 observed inclination angles for the X-axis, show that no significant fluctuations occurred
311 during the resting periods before and after the inclination was applied. The largest

deviation during these resting periods was 0.0015º (transmission count 8), with all other deviations remaining within 0.001º. During the adjustment periods, the maximum deviation observed was 0.001º (transmission counts 22, 29, 31).

The Type B results (Figure 15b), also corresponding to the X-axis and evaluating the deviation between applied and observed inclination angles, confirmed a clear linear correlation. The standard deviation (3σ), calculated using Eq. (3), was 0.0010º. These results indicate that tilt sensor A provided stable and highly accurate measurements throughout both resting and adjustment periods, successfully detecting changes as small as 0.001º. The detailed results for tilt sensors B through G are provided in Appendix A.

Table 2. Summary of experimental results

Tilt sensor	Resolution	Transmission Frequency	Installation Type	Communication Protocol	**Accuracy in X-axis(3 σ)**	**Accuracy in Y-axis(3 σ)**	**Accuracy in Z-axis(3 σ)**	**Rank**
A	0.001°	1 minute	Buried	LTE-M	**±0.0010°**	**±0.0014°**		**1**
B	0.003°	1 minute	Buried	LoRa	**±0.016°**	**±0.016°**		**7**
C	0.06°	15 minutes	Above Ground	Sigfox	**±0.040°**	**±0.063°**	**±0.068°**	**6**
D	0.005°	15 minutes	Buried	Sigfox	**±0.0090°**	**±0.0051°**		**4**
E	0.001°	2 minutes	Above Ground	LoRa	**±0.0021°**	**±0.0018°**		**2**
F	0.0002°	1 minute	Above Ground	ZETA	**±0.0074°**	**±0.0022°**	**±0.0034°**	**3**
G	0.1°	30 minutes	Above Ground	Sigfox	**±0.17°**			**8**
H	0.01°	5 minutes	Buried	NB-IoT	**±0.0090°**	**±0.010°**		**5**

330

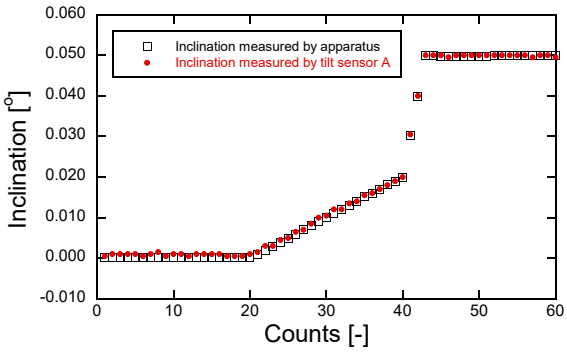


Figure 15a. Result Type A (X-axis from Tilt Sensor A)

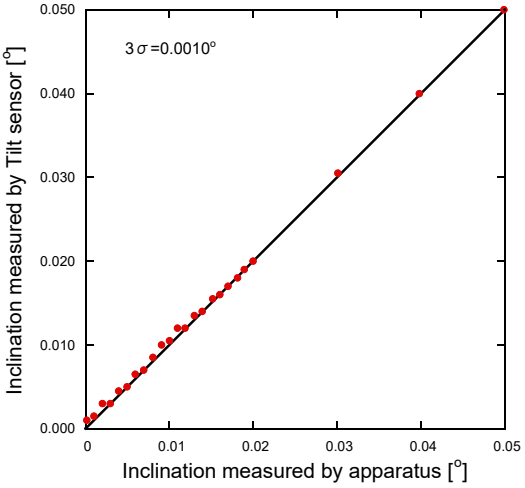


Figure 15b. Result Type B (X-axis from Tilt Sensor A)

4. Field Evaluation of LPWA Tilt Sensors

4.1. Overview of Field Observations

To evaluate the performance of tilt sensors under field conditions, devices incorporating different LPWA communication protocols and specifications were deployed on natural slopes for monitoring purposes. This chapter presents the annual observation results obtained from the eight Tilt sensors (Sensors A to H) described in Chapter 2.

The field experiments involving the eight Tilt Sensors were conducted at three sites. Tilt Sensors A and C were installed at Site W, Tilt Sensors B, D, and G at Site M, and Tilt

341 Sensors E, F, and H at Site A. For Site M, data collected during the year 2023 are presented,
342 whereas for Sites A and W, data from the year 2024 are reported. The details are
343 summarized in Table 3 . In addition, photographs showing the actual installation of the
344 tilt sensors in the field are presented in Figure 16 to illustrate the site conditions and
345 installation setup.
346



Figure 16. Field Setup and Installation Examples of the Tilt Sensors

Table 3. Tilt Sensor Types by Area and Site

Site	Rain gauge	Tilt sensor							
		A	B	C	D	E	F	G	H
W	Japan Meteorological Agency	●		●					
M	Rain gauge (Company B)		●		●			●	
A	Rain gauge (Company D)					●	●		●

4.2. Field Monitoring on Actual Slopes Using Each Tilt Sensor

To investigate the effects of external factors such as temperature, rainfall, animals, and natural disasters on monitoring performance, field observations were conducted at Site M and Site W in Ehime Prefecture, and Site A in Tokushima Prefecture.

The data obtained were analyzed using three approaches:

1. **Long-term trends of composite tilt angles:** X- and Y-axis tilt data were converted into a composite tilt angle using Eq. (7) and plotted alongside rainfall data to examine long-term trends.

2. **Inclination rate analysis:** Tilt velocities were calculated using Eq. (8) and graphed together with rainfall data. Since cumulative tilt alone may not provide a reliable indicator of collapse risk due to differences in Tilt Sensor installation timing, inclination rate offers a more quantitative assessment. As slope failure approaches, tilt velocities increase, making this parameter a more critical indicator.
3. **Temperature-induced variation:** To evaluate the influence of temperature on the tilt sensors at each site, a three-day period without rainfall was selected and plotted. The variability in measurements during this period was treated as temperature-induced error, and the standard deviation was included in the graphs to quantify temperature-related changes.

For all analyses, initial values were zero-offset using Eq. (4) to plot subsequent changes. Data points clearly affected by tilt sensor errors, such as battery failure or communication loss, were excluded from the analysis.

$$\Delta\boldsymbol{\theta_n} = \boldsymbol{\theta_n} - \boldsymbol{\theta_0} \quad (\boldsymbol{n} = \mathbf{1.2.3} \ldots) \tag{4}$$

Where $\Delta\theta_n$ [º] is the deviation from the initial tilt angle at the n-th observation, θ_n [º] is the tilt angle at the n-th observation, and θ_0 [º] is and initial tilt angle.

The tilt angles observed by the tilt sensor along the X and Y axes are determined by the installation setup, whereas the natural direction of slope movement often involves

deformation components along both axes. Therefore, a method for calculating a composite tilt angle that incorporates both components is presented.

Figure 17 illustrates the case where the tilt sensor inclines to a composite angle φ including both X- and Y-axis components. To clarify the calculation process, the scenario has been converted into a diagrammatic representation. From this figure, the angle AOC = φ can be determined.

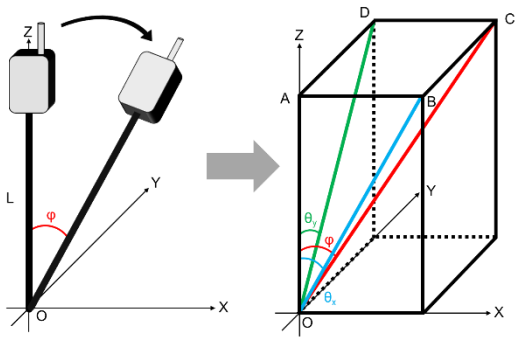


Figure 17 Schematic representation of the tilt sensor tilting

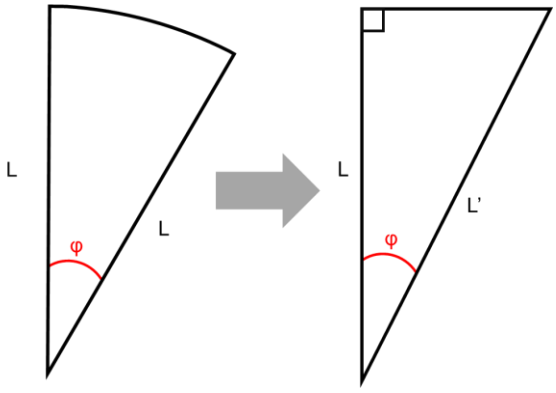


Figure 18 Approximation of the figure

As shown in Figure 18, when the composite tilt angle is extremely small, the lengths L and L′ can be considered approximately equal, allowing the left diagram to be treated as the right diagram. Accordingly, the length AC in Figure 17 can be calculated using the Pythagorean theorem, as expressed in Eq. (5).

$$\mathbf{AC} = \boldsymbol{l}\sqrt{\boldsymbol{sin^2\theta_x + cos^2\theta_y}} \tag{5}$$

Considering triangle OCA, tan φ can be expressed as shown in Eq. (6).

$$\boldsymbol{tan\varphi} = \frac{\boldsymbol{l}\sqrt{\boldsymbol{sin^2\theta_x + cos^2\theta_y}}}{\boldsymbol{l}} \tag{6}$$

Thus, the composite tilt angle φ can be determined as follows:

$$\boldsymbol{\varphi} = \boldsymbol{tan^{-1}}\sqrt{\boldsymbol{sin^2\theta_x + cos^2\theta_y}} \tag{7}$$

Where φ [°] is the composite tilt angle, θ_x [°] the is tilt angle in the X direction, θ_y [°] is the tilt angle in the Y direction, the L [m] is the tilt sensor length.

Inclination rate is then derived using:

$$\boldsymbol{\alpha} = \frac{\boldsymbol{\varphi_i - \varphi_{i-1}}}{\boldsymbol{t_i - t_{i-1}}} \quad (\boldsymbol{i = 1.2.3} \ldots) \tag{8}$$

Where α [°/h] is the inclination rate at the i-th observation, φ_i, φ_{i-1} [°] are the composite tilt angles at current and previous observations, and $t_i - t_{i-1}$ [h] is the time between observations.

Tilt sensors C at Site W, D and G at Site M, and E and H at Site A are provided in Appendix B.

393

394 **4.3. Site W**

395 Site W is equipped with Tilt Sensors A and C; however, the field observation results
396 of Tilt Sensors C are described in Appendix B. Tilt Sensor A (Figures 19 to 21): Figure
397 19 presents one year of observation records from Tilt Sensor A in terms of tilt angles and
398 rainfall. From around June, marking the beginning of the rainy season, through September,
399 the peak of the typhoon season, rainfall was particularly concentrated, and corresponding
400 increases in tilt angles can be observed. In contrast, during periods without rainfall, tilt
401 angles exhibited stable behavior. Around day 240, an increase in tilt angle is evident. The
402 rainfall event beginning on day 237 was caused by Typhoon No. 10 of 2024, with a
403 cumulative rainfall of 283 mm. Similarly, the rainfall event on day 193 produced a daily
404 rainfall of 71.5 mm, during which an increase in inclination rate was observed, while on
405 day 266, a rainfall of 81.5 mm resulted in a sharp increase in tilt angle.

406 Figure 20 illustrates the relationship between inclination rate and rainfall. Excluding
407 the tilt angle increases associated with rainfall, the one-year observation period remained
408 stable, with no exceedance of the Level 1 warning threshold of 0.02°/h. Conversely,
409 during rainfall events, inclination rate exceeded 0.02°/h, indicating elevated risk, although
410 it never surpassed 0.1°/h.

411 Figure 21 shows the change in inclination over a three-day period without rainfall,

412 in order to examine potential noise caused by temperature fluctuations. Since Tilt Sensor

413 A is a buried-type tilt sensor, it was minimally affected by temperature variations.

414

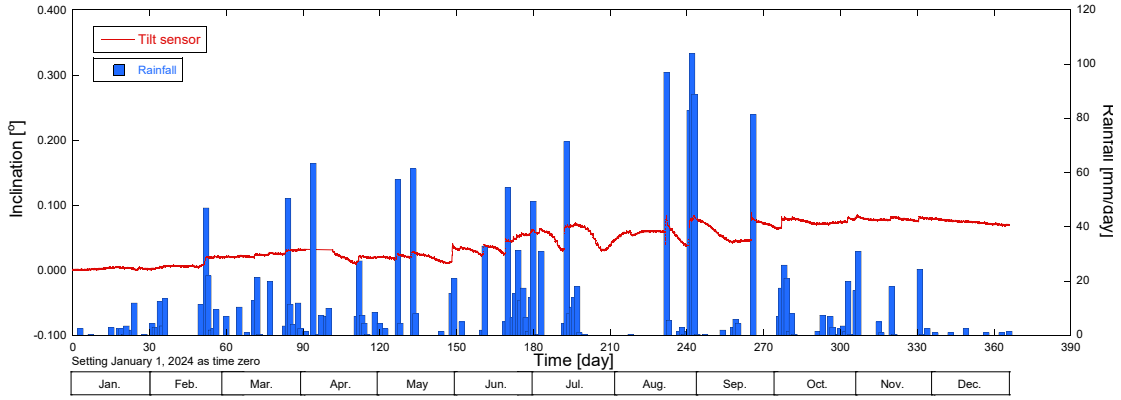


Figure 19. Composite Angle vs. Rainfall (Tilt Sensor A)

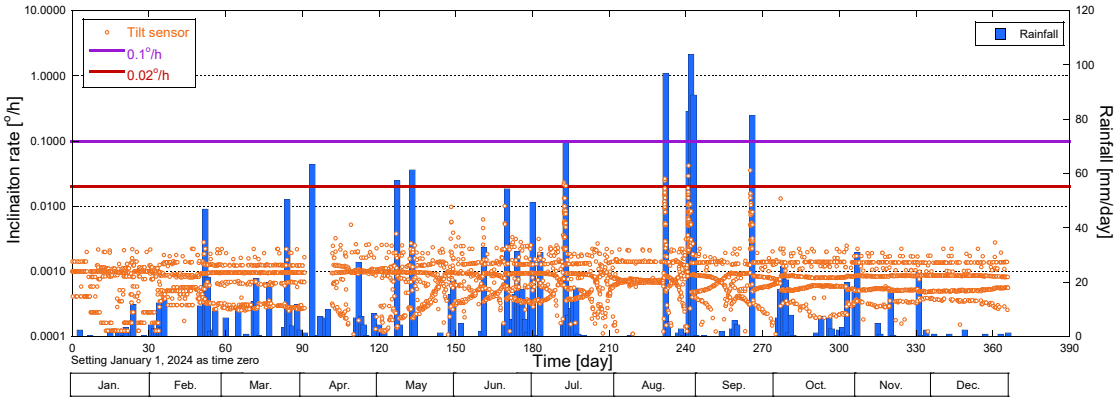


Figure 20. Inclination rate vs. Rainfall (Tilt Sensor A)

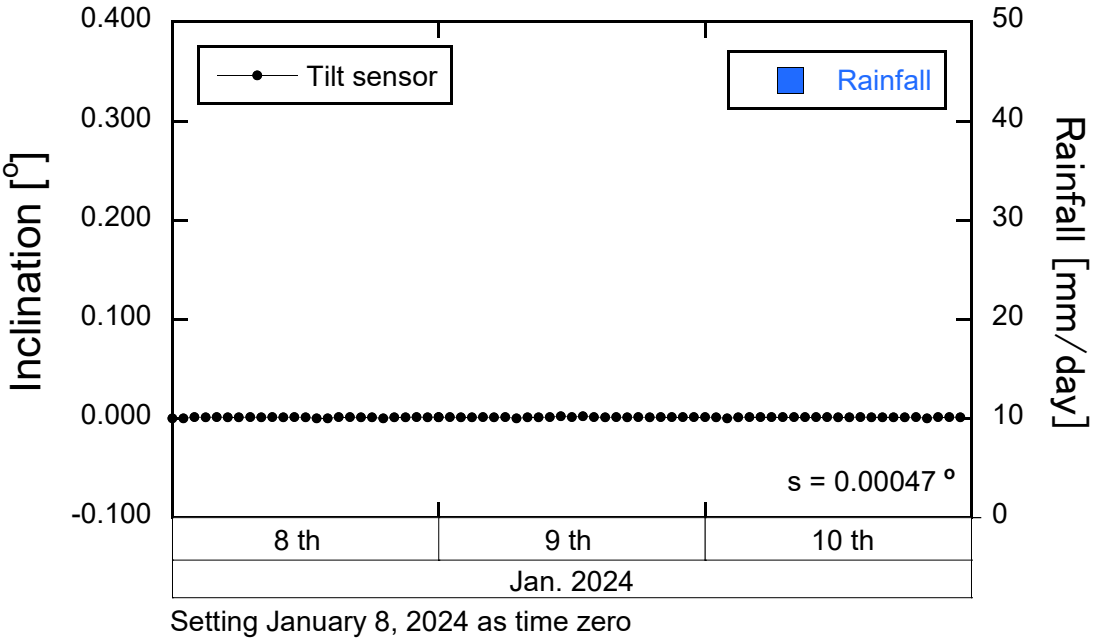


Figure 21. Effect of Temperature (Tilt Sensor A)

415

416 **4.4. Site M**

417 Site M is equipped with Tilt Sensors B, D, and G; however, the field observation

418 results of Tilt Sensors D and G are described in Appendix B.

419 Tilt Sensor B (Figures 22 to 24):

420 Figure 22 presents one year of observation records from Tilt Sensor B in terms of

421 tilt angles and rainfall. After the rainfall event of 54 mm on day 321, a gradual increase

422 in inclination was observed. Subsequently, the inclination remained stable without further

423 increase. This indicates that the deformation was not directly associated with each rainfall

event, but rather that the heavy rainfall acted as a trigger, accelerating slope movement irrespective of subsequent precipitation.

Figure 23 illustrates the relationship between inclination rate and rainfall. Tilt Sensor B consistently recorded values exceeding both 0.02°/h and 0.1°/h. However, since the resolution of the Tilt Sensor B is 0.010°, interpretation of rates around 0.02°/h is unreliable.

Figure 24 shows the change in inclination over a three-day period without rainfall. As shown in Figure 24, temperature-induced effects were more stable than those observed in Tilt Sensor C. This can be attributed to the underground installation design, similar to Tilt Sensor A, which reduces surface temperature influences. Nevertheless, Tilt Sensor B exhibited larger intrinsic noise than Tilt Sensor A, resulting in a greater standard deviation despite both being underground types.

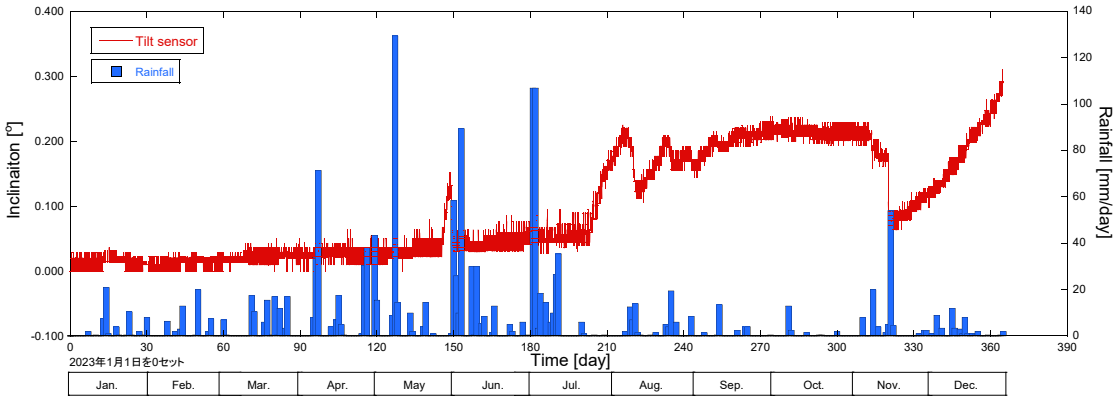


Figure 22. Composite Angle vs. Rainfall (Tilt Sensor B)

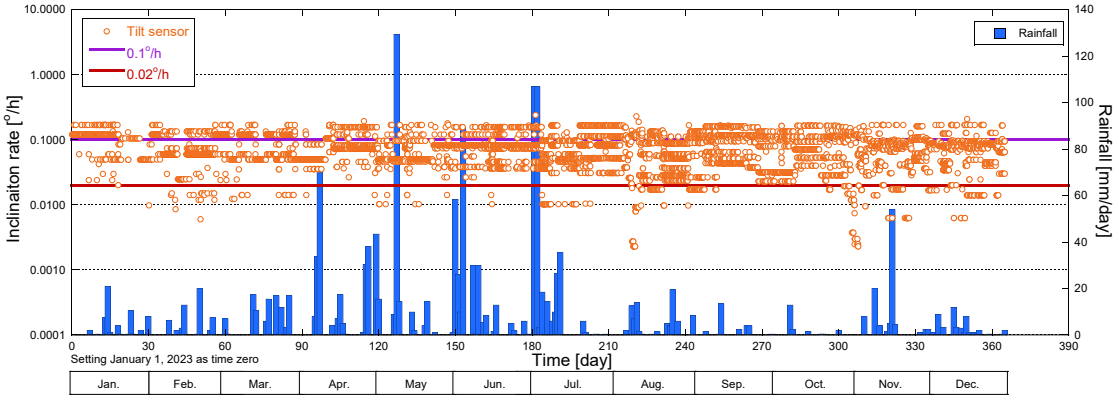


Figure 23. Inclination rate vs. Rainfall (Tilt Sensor B)

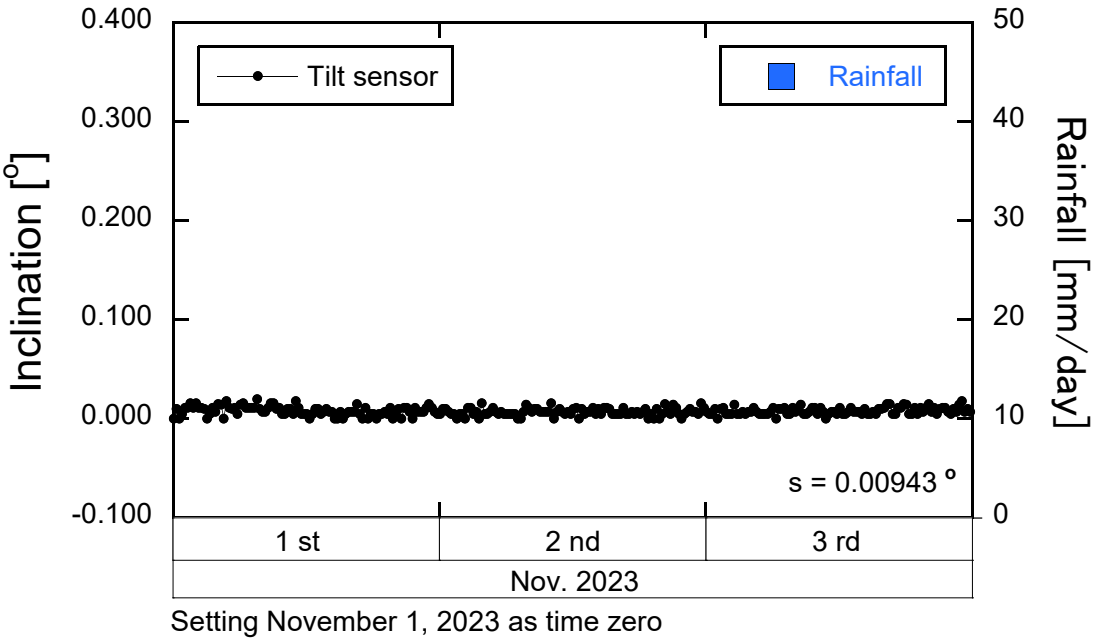


Figure 24. Effect of Temperature (Tilt Sensor B)

436

4.5. Site A

Site A is equipped with Tilt Sensors E, F, and H; however, the field observation results of Tilt Sensors E and H are described in Appendix B.

Tilt Sensor F (Figures 25 to 27):

Figure 25 presents one year of observation records from Tilt Sensor F in terms of tilt angles and rainfall. In Figure 25, Tilt Sensor F demonstrated a long-term increase in inclination throughout the year, with a cumulative change exceeding 20°. During the heavy rainfall event on day 149, a rapid increase in inclination was observed. Similarly, during the continuous rainfall over eight days from day 239, with a total of 303.8 mm, an increase in inclination was also recorded.

Figure 26 illustrates the relationship between inclination rate and rainfall. Figure 26 indicates that inclination rates increased during both the heavy rainfall on day 149 and the prolonged rainfall beginning on day 239, suggesting that slope deformation was detected by the Tilt Sensor F in response to rainfall. On day 119, a single data point exceeded 0.1°/h.

Figure 27 shows the change in inclination over a three-day period without rainfall. As illustrated in Figure 27, similar to other ground-based tilt sensors, inclination increased during the daytime and returned to its original value at night.

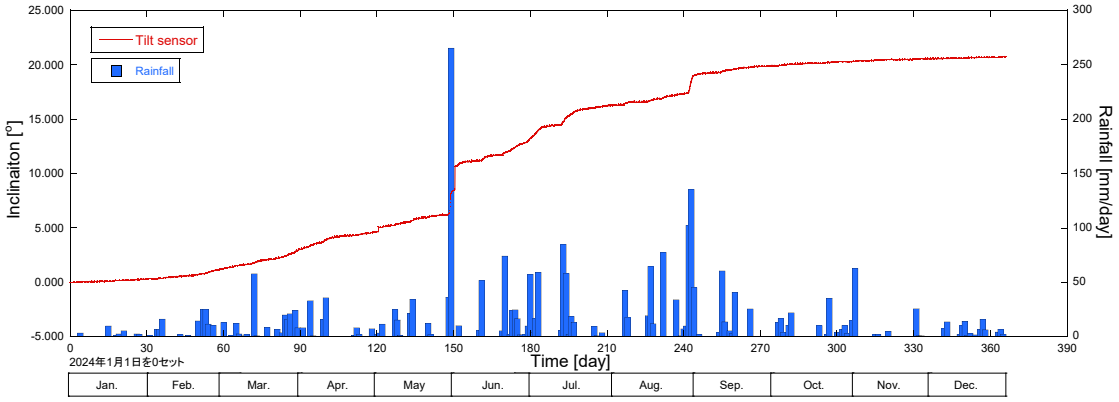


Figure 25. Composite Angle vs. Rainfall (Tilt Sensor F)

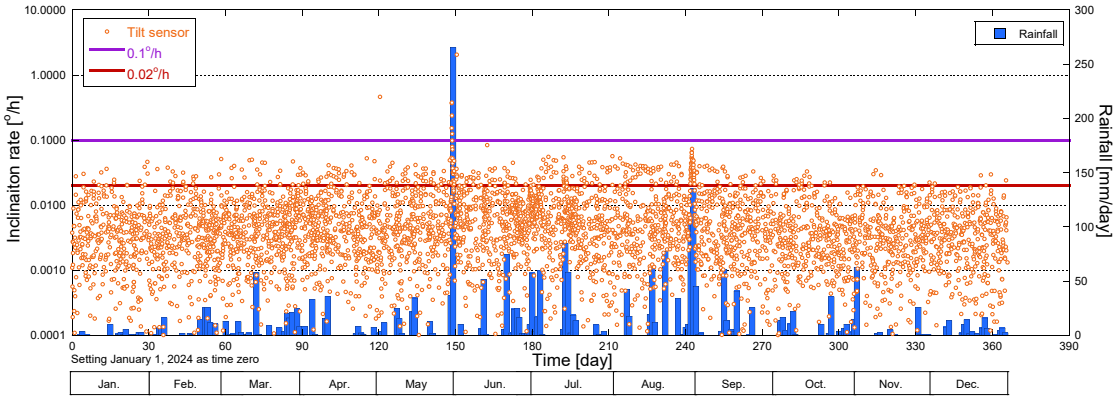


Figure 26. Inclination rate vs. Rainfall (Tilt Sensor E)

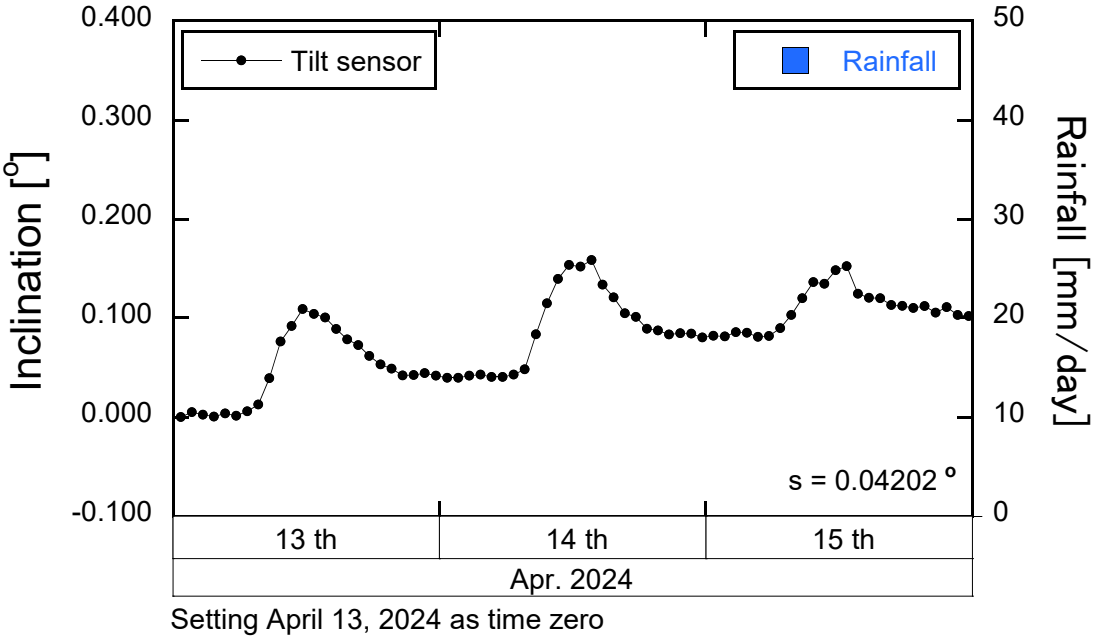


Figure 27. Effect of Temperature (Tilt Sensor F)

455

456 Table 4 summarizes the variability of inclination observed during three rain-free
457 days for each tilt sensor. The influence of temperature error was evaluated using the
458 standard deviation, and the sensors were ranked according to smaller standard deviation
459 values, representing smaller temperature errors. The ranking also incorporated the
460 accuracy confirmed in laboratory experiments. In the laboratory evaluation, the X-axis
461 was selected as the representative axis because it approximately corresponds to the
462 expected direction of slope deformation in the field, and therefore serves as a reference
463 axis for field observations. Figure 28 provides a graphical representation of Table 4,

combining both laboratory accuracy and field observation accuracy, with the error bars indicating 3σ derived from the laboratory results.

The measurement accuracy different among the tilt sensors, and the magnitude of the standard deviation reflected the degree of influence from temperature errors and sensor noise. The buried Sensors (A, B, D, and H) generally exhibited smaller standard deviations and thus produced more stable records. In contrast, the above-ground Sensors, particularly E, F, and G, showed larger standard deviations, indicating stronger susceptibility to external factors such as temperature fluctuations. Among them, Tilt Sensor G, which has the coarsest resolution (0.1°), displayed a wider range of values than the other sensors, confirming its lower measurement accuracy.

Table 4. Summary of Laboratory Accuracy and Field Observation Results

Tit sensor	Installation Type	Field Accuracy [º]	Rank (field)	Laboratory Accuracy in X-axis(3σ) [º]	Rank (lab)
A	Buried	0.00047	1	0.0010	1
B	Buried	0.00943	3	0.016	7
C	Above Ground	0.03318	6	0.040	6
D	Buried	0.00412	2	0.0090	4
E	Above Ground	0.03133	5	0.0021	2
F	Above Ground	0.04202	7	0.0074	3
G	Above Ground	0.16000	8	0.17	8
H	Buried	0.01860	4	0.0090	5

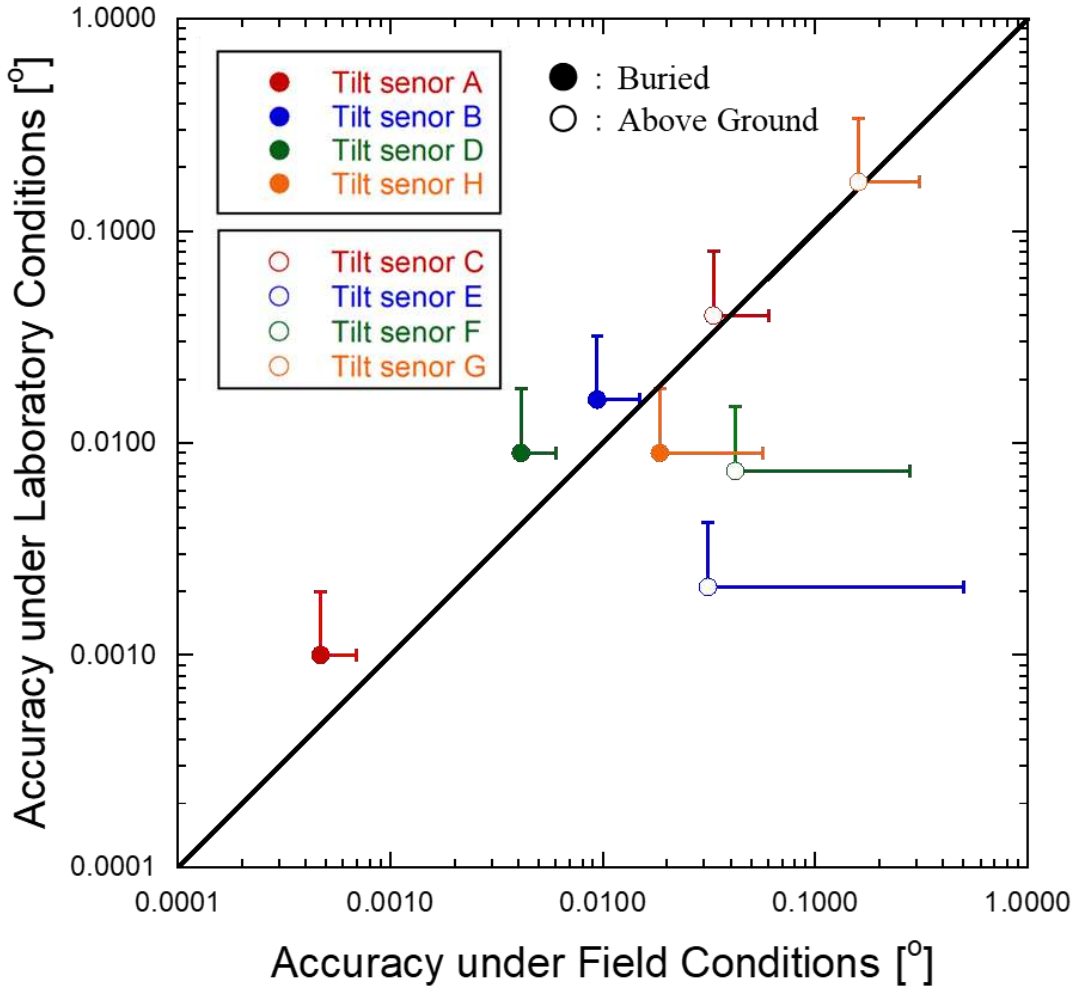


Figure 28. Summary of Laboratory Accuracy and Field Observation Temperature Errors

482

483 **4.6. Slope Failure at Site A**

484 On March 23, 2023, seven tilt sensors, excluding Sensor B, recorded a slope failure
485 at Site A. It should be noted that the sensors described in the previous section were
486 reinstalled after the slope failure and therefore represent different units from those that
487 actually recorded the event. Figure 29 presents the time-series variations of the composite

488 inclination angles of each sensor, with March 23, 2023, set as the zero reference point.
489 After the slope failure, the sensors toppled or were damaged, and thus their data were
490 excluded. For data exclusion, the maximum angular velocity observed by each tilt sensor
491 was assumed to represent the time of slope failure, and all subsequent data were removed
492 accordingly. Table 5 lists the maximum angular velocities and their corresponding times
493 recorded by each tilt sensor. As shown in Table 5, the times of slope failure observed by
494 the seven tilt sensors can be categorized into three main groups: around 17:00 on the 23rd,
495 around 18:30 on the 23rd, and around 07:00 on the 24th. Moreover, as shown in Figure
496 29, the initial stage of the slope failure exhibited a gradual increase in inclination angle,
497 corresponding to the primary creep stage. The inclination angle then accelerated
498 progressively, and immediately before the slope failure, the tertiary creep stage was
499 observed, ultimately leading to slope failure.

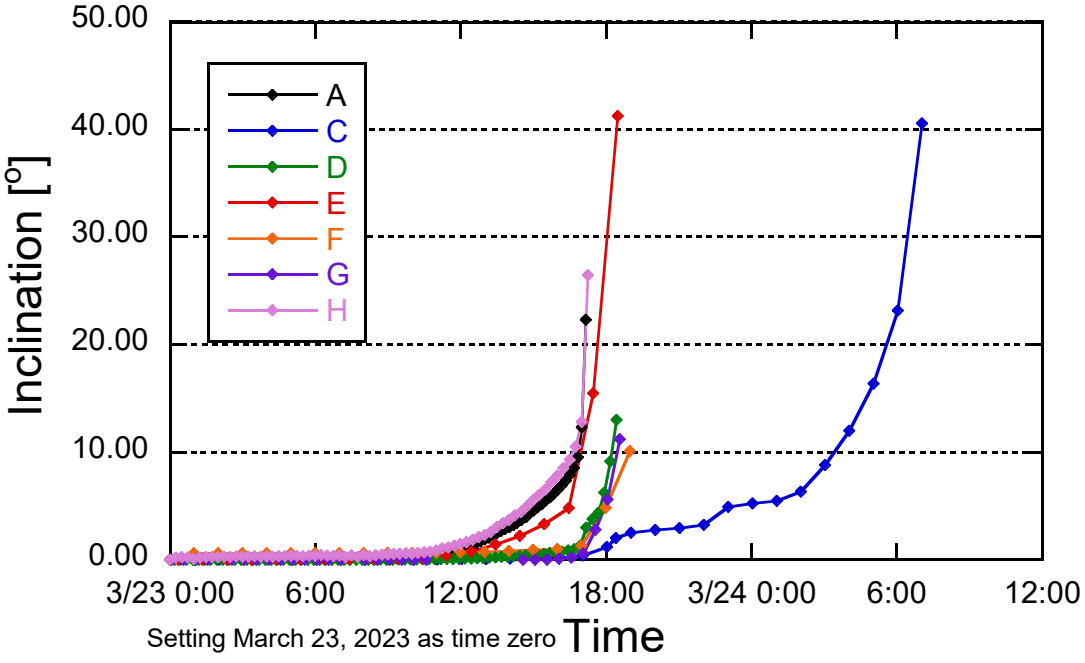


Figure 29. Temporal variation of composite inclination angle

Table 5. Maximum inclination rates observed by each tilt sensor and their corresponding times

Tilt sensor	Time	Max Inclination rate [°/h]
A	3/23 17:10	41.15
C	3/24 7:02	17.37
D	3/23 18:26	15.40
E	3/23 18:29	25.45
F	3/23 18:59	5.26
G	3/23 18:34	11.2
H	3/23 17:15	54.52

Figure 30 illustrates the relationship between the time until slope failure and the angular velocity of inclination. Although the times of slope failure shown in Table 5 can be classified into three groups, the tilt sensors exhibited similar tendencies, with angular velocity increasing as the slope failure approached. While some variability was observed among the tilt sensors, under the conservative assumption of the fastest slope failure scenario, the time until slope failure after exceeding 0.02°/h was approximately 7 hours, whereas once exceeding 0.1°/h, the time until slope failure was found to be less than 3 hours.

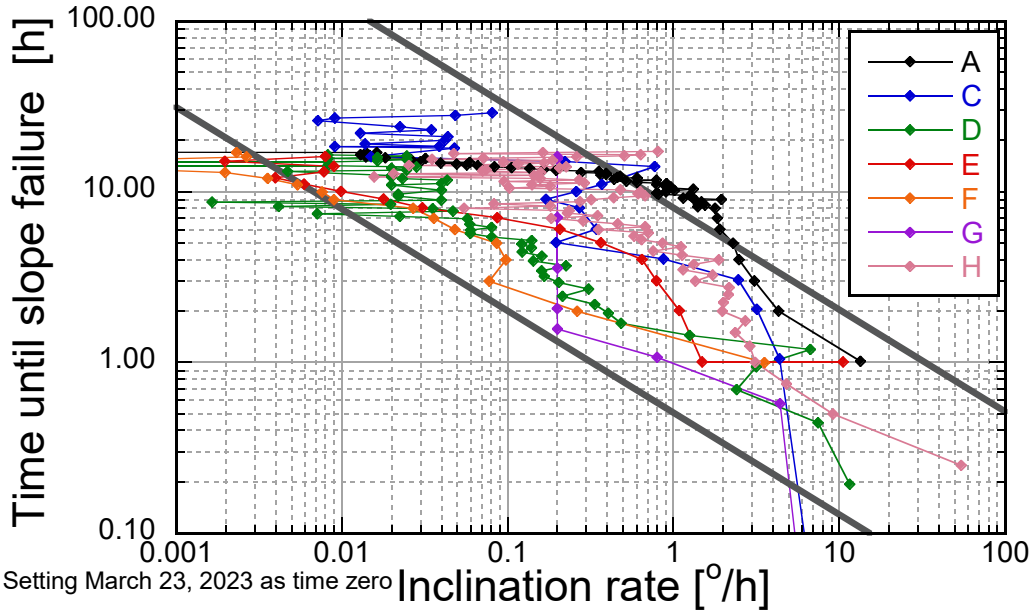


Figure 30. Relationship between Time until Slope Failure and Inclination Rate

508

509 Wang et al. (Wang et al. 2022) conducted analyses of past slope failure and

510 destabilization cases, the results of which are shown in Figure 31. From these results, they

511 derived Eq. (9), which expresses the remaining time to failure as a function of the angular

512 velocity of inclination.

$$\boldsymbol{log_{10}t_r = 0.306 - 0.597 log_{10}\frac{d\alpha}{dt} \pm 0.6} \quad (9)$$

513 Where $\boldsymbol{t_r}$ [h] is the remaining time to failure, $\frac{d\alpha}{dt}$ [°/h] is= angular velocity of inclination.

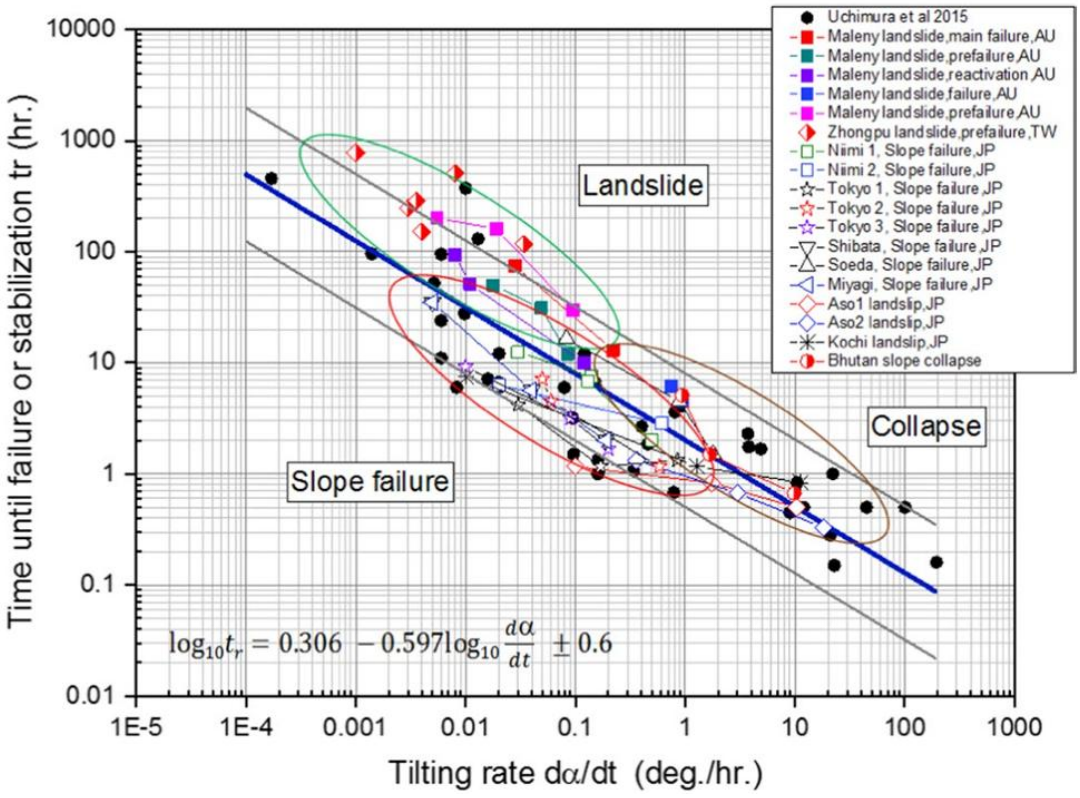


Figure 31. Relationship between Time until Slope Failure and Inclination Rate (quoted from Wang et al. (Wang et al. 2022))

514 Figure 32 shows the application of Eq. (9) to the results in Figure 30. A majority of
515 the plotted data points lie within the range predicted by the equation, demonstrating a
516 high degree of conformity with the relationship proposed in previous studies.
517 Consequently, the consistency of the slope failure events recorded by the seven tilt sensors
518 is substantiated.

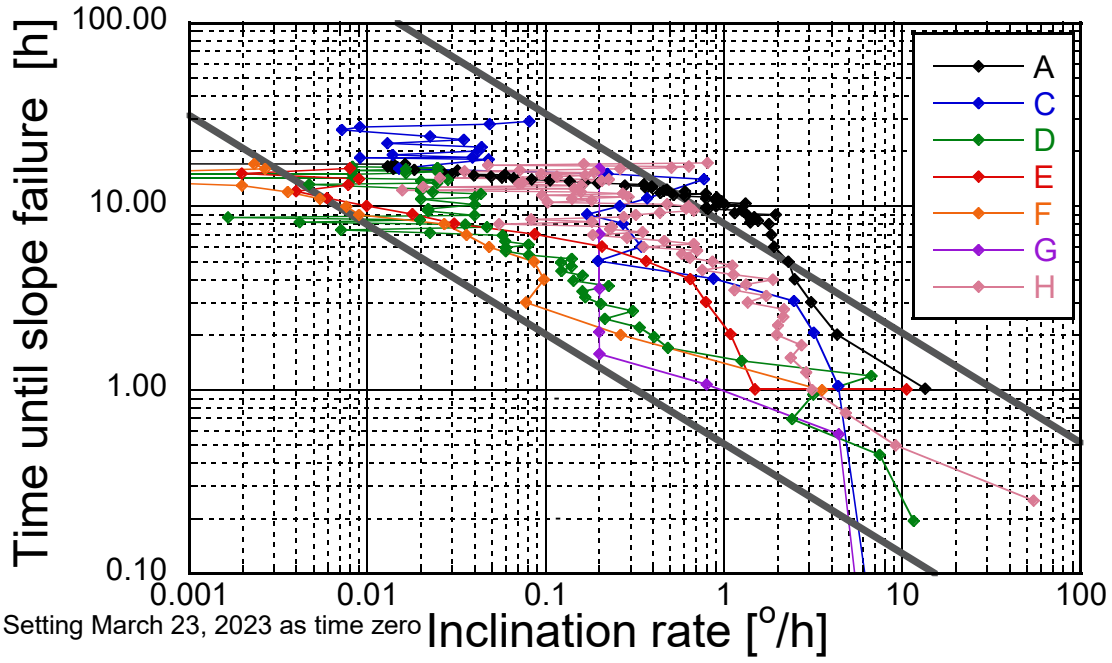


Figure 32. Relationship between Time until Slope Failure and Inclination Rate with Application of Eq. (9)

519

520 **4.7. Integration of Specifications and Field Performance**

521 The performance of tilt sensors is generally specified in catalog specifications such
522 as accuracy and resolution. However, it remains unclear to what extent these
523 specifications reflect tilt sensor stability and rainfall responsiveness under actual field
524 conditions. This section examines six Tilt Sensors (A, C, D, E, F, and G), focusing on the
525 relationship between accuracy and field-derived noise, as well as between resolution and
526 field-derived responsiveness. Tilt Sensors B and H were excluded from the analysis

because their installation sites were located far from the other tilt sensors, and this study aimed to minimize the influence of site-specific differences. The objective is to evaluate whether laboratory specifications can serve as reliable predictors of field performance. To this end, we first compute noise indices from tilt data and compare them with catalog accuracy and then derive responsiveness indices based on the correlation between tilt velocity and effective rainfall with varying half-lives and time lags. Regression analyses are subsequently conducted to quantify the strength of these relationships, and the results are presented in tables and figures to assess the predictive capability of catalog specifications.

4.7.1. Data and Methods

This study employed tilt angle and hourly rainfall data. Noise was evaluated using observations from 6–12 March 2023, when rainfall was relatively low, and responsiveness was assessed using observations from 17–20 March 2023, when rainfall was relatively high. Because sampling intervals varied among tilt sensors, all data were resampled to hourly resolution, with missing values shorter than six hours linearly interpolated and longer gaps excluded from analysis. As a result of this preprocessing, 145 data points were obtained for noise and 73 for responsiveness. For noise evaluation, tilt velocity $v(t)$

545 was calculated, and a five-hour median filter was applied to extract the trend component

546 $T(t)$. Residuals were then computed as $r(t) = v(t) - T(t)$, and their standard deviation

547 was defined as the noise index:

$$\sigma_r = \sqrt{\frac{1}{N}\sum (r(t) - \bar{r})^2} \tag{10}$$

548 where N denotes the number of residual data points used in the calculation. Smaller

549 values of σ_r indicate higher stability of tilt sensor output.

550 For responsiveness, tilt velocity was smoothed using a five-hour moving average ($\bar{v}(t)$)

551 and compared with effective rainfall $E_M(t)$, defined as:

$$\mathrm{E}_M(\mathrm{t}) = \mathrm{E}_M(\mathrm{t} - \Delta\mathrm{t})\, \mathrm{e}^{\beta\Delta\mathrm{t}} + \mathrm{R}(\mathrm{t})\, \mathrm{e}^{\frac{1}{2}\beta\Delta\mathrm{t}},\ \beta = \ln(0.5) / \mathrm{M} \tag{11}$$

552 where $R(t)$ is the hourly rainfall and M is the half-life, with β being converted from

553 the half-life M(Ito et al. 2020).

554 The responsiveness index (RI) was defined as the maximum absolute correlation

555 coefficient across all combinations of lag τ $(0 - 24\ h)$ and half-life M $(1 - 72\ h)$

$$RI = \max(\mathrm{M}, \tau)\, |\rho(\bar{v}(\mathrm{t}),\ \mathrm{E}_M(\mathrm{t} + \tau))| \tag{12}$$

$$\rho\ (\mathrm{X}, \mathrm{Y}) = \frac{\sum\ (\mathrm{X_i} - \bar{X})(\mathrm{Y_i} - \bar{Y})}{\sqrt{\sum (\mathrm{X_i} - \bar{X})^2}\ \sqrt{\sum\ (\mathrm{Y_i} - \bar{Y})^2}} \tag{13}$$

556

557 **4.7.2. Results**

558 The calculated indices of noise and responsiveness are summarized in Table 6 and
559 Table 7, respectively. Noise, defined as the standard deviation of residuals σ_r, represents
560 the stability of tilt sensor output, with smaller values indicating greater stability.
561 Responsiveness, defined as the maximum correlation coefficient RI, reflects the strength
562 of tilt sensor response to rainfall.

Table 6. Catalog accuracy and field-derived noise of tilt sensors

Tilt sensor	Accuracy[º]	Noise(σ_r)
A	0.0010 º	0.00053 º
C	0.04 º	0.0388 º
D	0.0018 º	0.0047 º
E	0.0018 º	0.00333 º
F	0.0022 º	0.00475 º
G	0.17 º	0.0535 º

Table 7. Catalog resolution and field-derived responsiveness indices of tilt sensors

Tilt sensor	Resolution	RI	Lag(h)	M(h)
A	0.001º	0.618	0	13
C	0.06º	0.228	2	1
D	0.005º	0.379	5	72
E	0.001º	0.631	8	72
F	0.0002º	0.240	3	31
G	0.1º	-0.191	23	12

563

564 **Accuracy and Noise**

565 As shown in Table 6, tilt sensors with higher catalog accuracy exhibited smaller noise.
566 Tilt Sensor A recorded the lowest noise (0.00053°), whereas Tilt Sensor G showed the
567 highest (0.0535°). Figure 33 illustrates this relationship with the x-axis plotted on a
568 logarithmic scale. The regression line is given as ($Y = 0.025X + 0.073$) where $X =$
569 $log(accuracy[°])$. The coefficient of determination is $R^2 = 1.00$, indicating an almost
570 perfect linear relationship in the log-transformed domain. This result demonstrates that
571 catalog accuracy is an excellent predictor of field stability.

572

Resolution and Responsiveness

In contrast, Table 7 reveals that resolution and responsiveness do not exhibit a simple proportional relationship. Tilt Sensor E (resolution = 0.001°) showed the highest responsiveness ($RI = 0.631, M = 72, lag = 8\,h$), whereas the highest-resolution sensor, Tilt Sensor F (resolution = 0.0002°), yielded an RI of only 0.240. Figure 34 depicts the regression line ($Y = -6.167X + 0.489$) with a coefficient of determination of $R^2 = 0.73$, suggesting a moderately strong negative linear trend between resolution (higher values indicating coarser sensors) and responsiveness. However, exceptions such as Tilt Sensor F, which combines high resolution with relatively low responsiveness, indicate that site conditions and sensor-specific factors also play an important role.

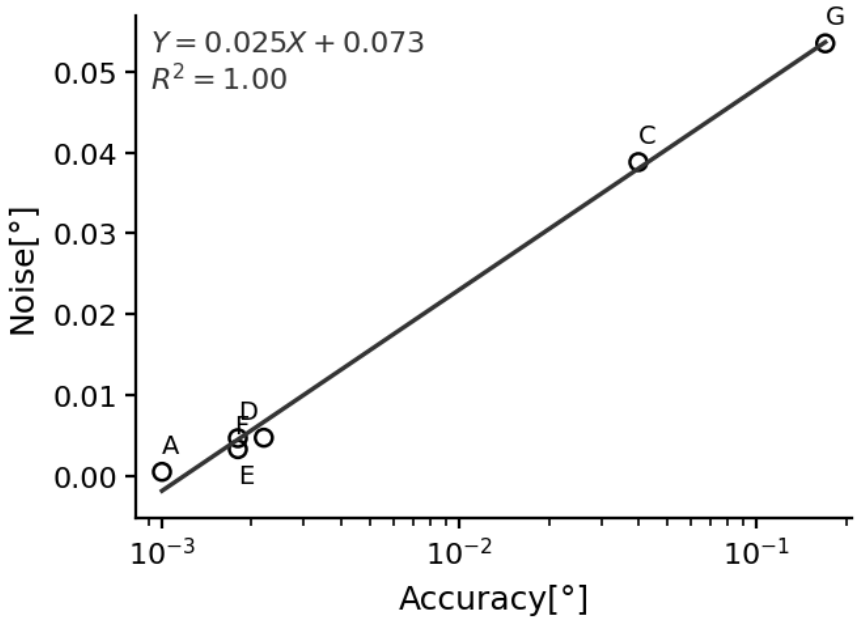


Figure 33: Relationship between catalog accuracy and field-derived noise

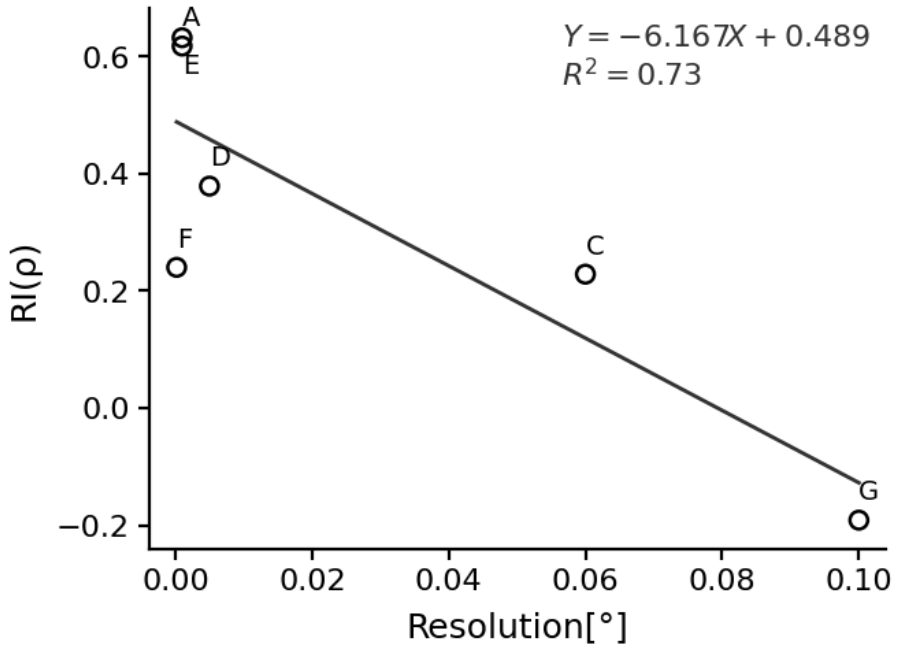


Figure 34: Relationship between catalog resolution and field-derived responsiveness

583

584 **4.7.3. Discussion**

585 From these results, two key findings can be drawn:

586 • **Accuracy is a reliable predictor of noise.**

587 A strong linear relationship between catalog accuracy and field-derived noise

588 demonstrates that laboratory accuracy specifications reliably reflect field stability.

589 • **Resolution is not a reliable predictor of responsiveness.**

590 Higher resolution does not guarantee greater rainfall responsiveness. External

591 factors, such as installation conditions and sensor-specific variability, likely exert a

592 stronger influence on responsiveness than catalog resolution alone.

593 Overall, the results demonstrate that catalog accuracy reliably predicts field noise
594 levels, confirming that accuracy specifications provide a meaningful indicator of sensor
595 stability under real monitoring conditions. In contrast, catalog resolution does not
596 consistently predict rainfall responsiveness, indicating that responsiveness is strongly
597 influenced by installation conditions and sensor-specific characteristics. These findings
598 highlight the importance of prioritizing proven accuracy and considering site-dependent
599 factors when selecting and deploying tilt sensors for slope monitoring.
600
601 **5. Conclusions**
602 This study investigated the practical applicability of LPWA-based surface tilt sensors
603 for slope monitoring through both laboratory experiments and field observations. Based
604 on the results, the main findings are summarized as follows:
605 1. Laboratory Evaluation of Tilt Sensors:
606 Identical tilt angle profiles were applied to multiple LPWA-based surface tilt
607 sensors using a testing device. The sensors were quantitatively evaluated based on
608 their ability to detect tilt changes at a resolution of 0.001°, with performance
609 variations assessed using standard deviation. Some tilt sensors demonstrated high

sensitivity, while others exhibited limited tracking performance due to resolution and accuracy constraints.

2. Field Observation and Rainfall Correlation:

   One year of continuous monitoring data for tilt angle and angular velocity were analyzed in relation to rainfall. Results indicated that:

   - Increased rainfall led to larger tilt angles, elevating the risk of slope failure.
   - During periods of low precipitation, tilt angles tended to return to pre-rainfall levels.
   - Most tilt sensors recorded angular velocities exceeding 0.02°/h, implying that only a few could be evaluated using the management threshold proposed by Tanikawa et al.

3. Temperature Effects:

   Buried tilt sensors were less affected by temperature fluctuations, providing more stable measurements compared to surface-installed tilt sensors.

4. Slope Failure Detection at Site A:

   Seven tilt sensors successfully captured the occurrence of a slope failure. The increases in tilt angle and angular velocity were clearly observed. The relationship

between remaining time until failure and angular velocity was consistent with previous studies.

5. Validation of Laboratory Indicators for Field Use:

Regression analysis confirmed that laboratory-derived indicators were effective for evaluating field performance, demonstrating the practical applicability of LPWA-based tilt sensors for long-term slope monitoring.

637 **Acknowledgements**

638 This work was financially supported by Ehime Prefecture through the Digital
639 Implementation Acceleration Project “TRY ANGLE EHIME.” The authors gratefully
640 acknowledge the companies that conducted inclinometer measurements and provided
641 technical cooperation (in alphabetical order): Asano Taiseikiso Engineering Co., Ltd.,
642 Chuo Kaihatsu Corporation, Nishimatsu Construction Co., Ltd., Osasi Technos Inc.,
643 OYO Corporation, RYODEN Corporation, Satori Electric Co., Ltd., and TOPPAN Inc.
644 The authors also thank the following organizations for their additional cooperation and
645 support (in alphabetical order): Dia Nippon Engineering Consultants Co., Ltd., Lime
646 Consultant Co., Ltd., 923 Solutions, National Institute of Occupational Safety and Health,
647 Japan (JNIOSH), Japan Organization of Occupational Health and Safety (JOHAS), and
648 Mitsui Sumitomo Insurance Co., Ltd.

649 **Funding**

650 This research was financially supported by Ehime Prefecture through the Digital
651 Implementation Acceleration Project “TRY ANGLE EHIME.”

652 **Data Availability**

653 The data that support the findings of this study are available from the corresponding
654 author upon reasonable request.

Declarations

Conflict of interest: The authors declare no competing interests.

References

Ehime University (2023) FY2023 Project Report

Horton RE (1945) Erosional Development of Streams and Their Drainage Basins; Hydrophysical Approach to Quantitative Morphology. GSA Bulletin 56:275–370. https://doi.org/10.1130/0016-7606(1945)56%255B275:EDOSAT%255D2.0.CO;2

Ito N, Ito Y, Tamato S (2005) Development of a Real-Time Monitoring System for Landslide Movement Using Global Navigation Satellite System. In: Proceedings of the 11th International Conference and Field Trip on Landslides.

Ito S, Oda K, Koizumi K, Sako I (2020) Applicability of Recurrent Neural Networks to Prediction of Field-Measured Volumetric Water Content. Journal of Japan Society of Civil Engineers 76:

Japan Meteorological Agency (2024) Climate Change Monitoring Report 2023. Japan Meteorological Agency

672 Mekki K, Bajic E, Chaxel F, Meyer F (2019) A Comparative Study of LPWAN
673 Technologies for Large-Scale IoT Deployment. ICT Express 5:1–7.
674 https://doi.org/10.1016/j.icte.2017.12.005

675 Ministry of Land, Infrastructure, Transport and Tourism (2025) Sediment Disasters in
676 Japan in 2024. Ministry of Land, Infrastructure, Transport and Tourism

677 National Institute for Land and Infrastructure Management (2016) Manual of Technical
678 Standards for Establishing Sabo Master Plans for Debris Flow and Driftwood.
679 Ministry of Land, Infrastructure, Transport and Tourism

680 Sheikh MR, Nakata Y, Shitano M, Kaneko M (2021) Rainfall-Induced Unstable Slope
681 Monitoring and Early Warning Through Tilt Sensors. Soils and Foundations
682 61:1033–1053. https://doi.org/10.1016/j.sandf.2021.05.010

683 Takayuki N (2021) Research on Increasingly Severe and Frequent Sediment Disasters
684 and Their Countermeasures. National Institute for Land and Infrastructure
685 Management

686 Tanigawa M, Slope Monitoring Market Development Consortium (2024) Examination of
687 Slope Deformation and Failure Processes Using IoT Tilt Sensors and a

688 Provisional Proposal of Management Threshold Values. In: Proceedings of the
689 Japan Federation of Geotechnical Consultants Associations Technical Forum
690 2024. Niigata

691 TryAngle Ehime (2023) Ehime Disaster Prevention 2024: Thinking About Disaster
692 Management in Ehime. In: note（ノート）.
693 https://note.com/tryangle_ehime/n/nc4d7ace4c600. Accessed 13 Feb 2026

694 Tsukamoto Y (1973) Study on the Relationship Between Landslides Caused by Heavy
695 Rainfall and the Growth of Stream Channels (I). 25:4–13

696 Tsukamoto Y, Hiramatsu S, Shinohara S (1973) Study on the Growth of Stream Channels
697 (III): Relationship Between Zero-Order Valleys and Landslides. 26:14–20

698 Turner AK, Schuster RL (eds) (1996) Landslides Investigation and Mitigation. National
699 Research Council, Washington, DC

700 Uchimura T, Towhata I, Wang L, et al (2015) Precaution and Early Warning of Surface
701 Failure of Slopes Using Tilt Sensors. Soils and Foundations 55:1086–1099.
702 https://doi.org/10.1016/j.sandf.2015.09.010

Wang L, Seko I, Fukuhara M, et al (2022) Risk Evaluation and Warning Threshold of Unstable Slope Using Tilting Sensor Array. Nat Hazards 114:127–156. https://doi.org/10.1007/s11069-022-05383-y

Yoshimura C, Omura T, Furumai H, Tockner K (2005) Present State of Rivers and Streams in Japan. River Research and Applications 21:93–112. https://doi.org/10.1002/rra.835

Supplementary Files

This is a list of supplementary files associated with this preprint. Click to download.

- SupplementaryInformationLPWApaper.docx